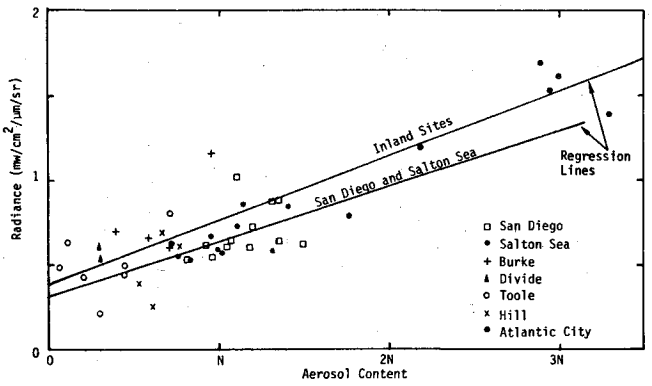

Fig. 3 Radiance vs aerosol content for MSS7 (radiances are normalized to nadir viewing and a sun zenith angle of 63 deg).

Four of the ground-truth sites are located in North Dakota and Montana; the fifth site is at Atlantic City, N.J. The target at Burke, N. Dak., is a river about 500 m wide and 300 m from the sunphotometer location; the Divide, N. Dak., target is a lake 2000×500 m at a distance 500 m from the sunphotometer site; the Toole, Mont., target is a lake 500×500 m at a distance 3000 m from the sunphotometer site; the Hill, Mont., target is a river about 1000 m wide and located about 8000 m from the sunphotometer site; and the Atlantic City target is a reservoir, approximately 300×2000 m, located about 2000 m from the sunphotometer site.

The MSS7 radiance-aerosol content relationship determined for these inland bodies of water is shown in Fig. 3. The San Diego and Salton Sea data for MSS7 are also shown in Fig. 3 (the Salton Sea is very large, being approximately 10×30 km, and is considered equivalent to an ocean target). Raw data tapes were not readily available for these sites, so only radiances for aerosol contents greater than $0.75N$ are shown, since analysis of the inland sites showed the radiance values at these aerosol contents to be about the same on both the calibrated and the raw tapes. The regression line for the inland data shows higher radiance values and more scatter of data than the regression line for the San Diego and Salton Sea data. These differences are mainly attributed to four possible factors, viz., errors in the sunphotometer data, differences in the aerosol properties among the sites, water turbidity effects, and the adjacency effect. These factors and others are discussed in detail by Griggs,[7] who concludes that most of the scatter in the data is caused by water turbidity effects. Little contribution is found from the adjacency effect, in contrast to the large contribution that is theoretically predicted.[8-10] The relationship shown in Fig. 3 can be used to estimate the aerosol content above inland bodies of water with a standard deviation of $0.42N$; this uncertainty is much greater than that found for MSS6 over the ocean ($0.12N$). It appears that the relationship for the inland bodies of water would best be applied to determining an average aerosol content over a period of time at a given target, or an area average at a given time over several targets close together. This averaging could reduce the uncertainty in the measured aerosol content to a useful level.

Conclusions

Linear relationships between the upwelling visible radiance and the aerosol content over the oceans have been found for several satellite sensors, and suggest that satellite monitoring of aerosols on a global basis is possible over the oceans. Use of the same technique for inland bodies of water does not look as promising for accurate measurements with single observations. However, averaging observations over space or time may prove to be useful for quantitative monitoring of pollution episodes over land.

Acknowledgments

This research has been supported by NASA Contracts NAS5-20899 and NAS1-15898, ONR Contract N00014-77-C-0489, and NOAA Contract MO-A01-78-00-4092.

References

[1] Griggs, M., "Measurements of Atmospheric Aerosol Optical Thickness over Water Using ERTS-1 Data," *Journal of Air Pollution Control Association*, Vol. 25, June 1975, pp. 622-626.

[2] Griggs, M., "Comment on 'Relative Atmospheric Aerosol Content from ERTS Observations,'" *Journal of Geophysical Research*, Vol. 82, Oct. 1977, p. 4972.

[3] Griggs, M., "Satellite Observations of Atmospheric Aerosols During the EOMET Cruise," *Journal of the Atmospheric Sciences*, Vol. 36, April 1979, pp. 695-698.

[4] Elterman, L., "Atmospheric Optics," *Handbook of Geophysics and Space Environments*, edited by S. Valley, McGraw-Hill Book Co., New York, 1965.

[5] Griggs, M., "Determination of Aerosol Content in the Atmosphere from Landsat Data," NASA-CR-155788, Jan. 1978.

[6] Dave, J. V. and Gazdag, J., "A Modified Fourier Transform Method for Multiple Scattering Calculations in a Plane Parallel Mie Atmosphere," *Applied Optics*, Vol. 9, June 1970, pp. 1457-1466.

[7] Griggs, M., "Satellite Measurements of Tropospheric Aerosols," Final Rept., NASA Contractor Rept. 3459, Aug. 1981.

[8] Turner, R. E., "Atmospheric Effects in Multispectral Remote Sensing Data," Environmental Research Institute of Michigan, Final Rept., NASA Contract NAS9-14123, May 1975.

[9] Pearce, W. A., "A Study of the Effects of the Atmosphere on Thematic Mapper Observations," EG&G Rept., NASA Contract NAS5-23639, Oct. 1977.

[10] Otterman, J. and Fraser, R. S., "Adjacency Effects on Imaging by Surface Reflection and Atmospheric Scattering: Cross Radiance to Zenith," *Applied Optics*, Vol. 18, Aug. 1979, p. 2852-2860.

AIAA 82-4017

A Probe for Low-Speed Measurements in Low-Density Flows

J. H. Brown* and R. E. Good†
Air Force Geophysics Laboratory, Hanscom Air Force Base, Mass.

Introduction

SOME environmental experiments conducted below stratospheric balloons require a determination of wind speed. The wind speed at the scientific package suspended several hundred meters below the balloon is a wind speed relative to the drifting balloon. This relative wind speed seldom exceeds 10 m/s. The aerodynamics of the probe at this low speed and low pressures (P= 1-60 Torr) represent unique conditions that have not been extensively investigated. Consequently, wind-tunnel measurements were recently conducted to determine the flow speed through open pipe probes. With the wind-tunnel calibration, the balloon-borne probe flow speeds are related to the freestream flow.

The calibration was conducted at the NASA Ames Martian Surface Wind Tunnel[1] that duplicated the stratospheric densities and low speeds encountered on a balloon. The tunnel wind speed was measured with a pitot probe. Pitot probe corrections for low Reynolds numbers were made using the data of Bryer and Pankhurst.[2]

Received Feb. 27, 1981. This paper is declared a work of the U. S. Government and therefore is in the public domain.

*Scientist, Aeronomy Division.
†Scientist, Aeronomy Division. Member AIAA.

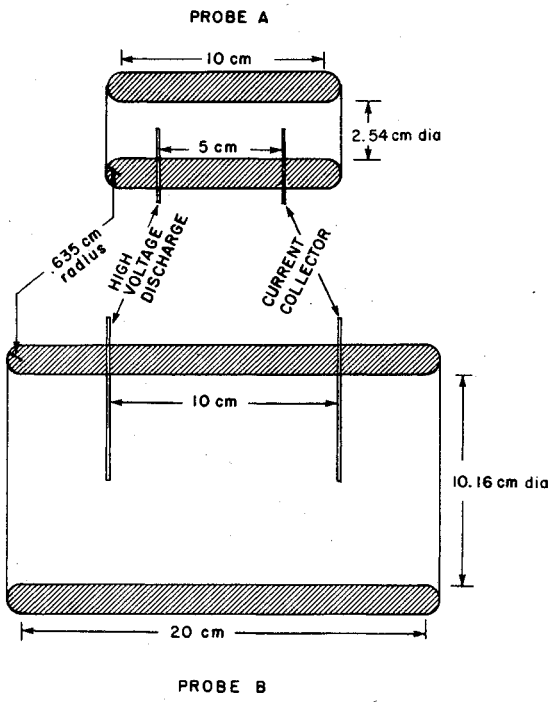

Fig. 1 Time-of-flight wind speed probes.

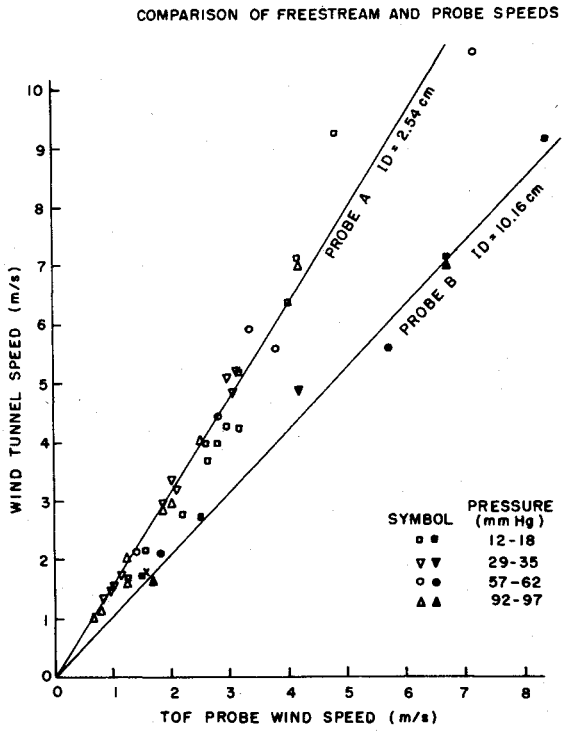

Fig. 2 Comparison of freestream and probe speeds.

Two probes were constructed having different inside diameters in order to determine the dependence of the internal flow speed on the wall thickness-to-diameter ratio. The internal speed was determined by observing the time-of-flight (TOF) of an ion cloud convected between the spark discharge and collector probes shown in Fig. 1. This technique was used by Lillienfeld[3] to determine the flow speed inside a sampling tube. The TOF probe developed here, when calibrated against freestream conditions, is a simple, trouble-free instrument suitable for stratospheric balloon-borne measurements.

Probe Description

The TOF wind speed probes consisted of short pipes with well-rounded entrances as shown in Fig. 1. The well-rounded probe essentially removes any entrance flow contraction. These probes were placed in the wind tunnel along side pitot probes that measured the wind-tunnel conditions. In the TOF probe, an ion cloud is produced every second at the high-voltage cathode and current collected downstream at a wire anode.

The ion cloud, produced by a spark discharge of 600-2000 V is convected downstream to the anode. The initial 75 μs discharge produces a Gaussian-shaped ion current distribution having typically a 10 ms half-width as it passes across the downstream anode. A peak detection circuit is used to determine the arrival time of the peak current. The flow velocity is determined simply as the distance divided by the time of flight. The actual current-time distribution is skewed by diffusion, but the error in peak time represents less than 0.1 m/s in speed.

Results

Measurements were conducted at the following wind-tunnel conditions: velocity, 1-20 m/s; pressure, 12-90 mm Hg; and temperature, ~300 K. The results are shown in Fig. 2.

Using the 10 cm (4 in.) diam probe, the TOF speed measurement V_i is nearly identical to the freestream speed V_∞

$$V_\infty = (1.06 \pm 0.26)\, V_i \quad \text{Probe B} \quad 10\text{ cm (4 in.) diam}$$

However, the 2.5 cm (1 in.) diam probe indicated considerably slower TOF speed

$$V_\infty = (1.60 \pm 0.37)\, V_i \quad \text{Probe A} \quad 2.5\text{ cm (1 in.) diam}$$

Discussion

The wind tunnel measurements were conducted over a Reynolds number range of 50-1500 based on the probe inside diameter d. Of the 71 data points, only 5 were at Reynolds numbers greater than 1000. An attempt was made to observe a Reynolds number dependence using data in the Reynolds number range of 100-900. No statistically significant Reynolds number dependence could be obtained that was an improvement over the straight line dependence on velocity shown above.

The velocity defect inside the probe is a result of the pressure forces on the inlet of the probe. Taking a momentum balance over a control volume surrounding the inlet,[4] the thrust on the inlet is $T = \frac{1}{2}\rho V_\infty^2 (1 - V_i/V_\infty)^2 \pi d^2/4$. The probe drag based on the frontal area is $D = \frac{1}{2}\rho V_\infty^2 \pi(d+t)tC_D$ where t is the probe wall thickness and C_D the drag coefficient. Equating the thrust and drag, the velocity defect can be determined to first order term as

$$\frac{\Delta V}{V_\infty} = \sqrt{4C_D \frac{t}{d}\left(1 + \frac{t}{d}\right)}$$

where $\Delta V = V_\infty - V_i$. Using the wind-tunnel measurements, the average value of the drag coefficient is 0.045 and 0.0057 for probes A and B, respectively. The results indicate that the internal flow speed approaches the freestream speed when the probe wall thickness-to-diameter ratio is less than 0.1. In order to also have a well-rounded entrance to avoid entrance effects and to minimize angle-of-attack effects, it is necessary to utilize a large diameter probe. Thus the time-of-flight speed measurement inside a large diameter, thin walled probe will measure the freestream speed.

Acknowledgments

The authors are indebted to suggestions and assistance provided by Edmond Dewan in reviewing the text, John Borghetti in conducting the measurements, and Ed Trzcinski for the design of the electronics. The support of Bill Borucki and Rod Leach of NASA Ames is greatly appreciated.

References

[1] White, B. R., "Low-Reynolds-Number Turbulent Boundary Layers," *Turbulent Boundary Layers: Forced, Incompressible, Non-Reacting,* edited by H. E. Weber, ASME, New York, 1979, pp. 209-220.

[2] Bryer, D. W. and Pankhurst, R. C., *Pressure-Probe Methods for Determining Wind Speed and Flow Directions,* National Physics Laboratory, Her Majesty's Stationary Office, London, 1971, p. 9.

[3] Lilienfeld, P., Solon, L., and DiGiovanni, H., "Ion Tracer Anemometer for the Measurement of Low Density Flows," *Review of Scientific Instruments,* Vol. 38, April 1967, pp. 405-409.

[4] Kuchemann, D. and Weber, J., *Aerodynamics of Propulsion,* 1st Ed., McGraw-Hill Book Co., New York, 1953, pp. 60-62.

AIAA 82-4018

Large Deflection of an Elliptic Plate under a Concentrated Load

B. Banerjee*

Jalpaiguri Government Engineering College, Jalpaiguir, India

Introduction

THIN plates of different shapes frequently occur in many structures. Thus the study of the bending properties of a plate is imperative to a design engineer. With the increased use of strong and lightweight structures, especially in aerospace engineering, many problems of nonlinear deformation naturally arise where the supplementary stresses in the middle plane of the plate must be taken into account in deriving the differential equations of plates.

Because plates in the shape of an ellipse sometimes occur in design, large-deflection analysis of such plates has attracted many eminent research workers. Weil and Newmark[1] and Nash and Cooley[2] have investigated the large deflections of elliptic plates using von Kármán's coupled equations. Both groups have used numerical methods to obtain their solutions. Mazumdar and Jones[3] have analyzed small deformations of elliptic plates by the method of constant-deflection contour lines. The authors have extended their method to the analysis of large deflections of elliptic plates[4] by applying the well-known Berger equations.[5] Another interesting paper by Dutta[6] needs special mention because he investigated the large deflection of a clamped orthotropic elliptic plate by completely solving the differential equation for the stress function. All of these investigations are confined to uniform loading only.

A survey of the literature on nonlinear deformation of elastic plates shows that apparently no paper has been devoted to an investigation of the large deflection of an elliptic plate under a concentrated load at the center. In this Note an attempt has been made to investigate this problem by the method of constant-deflection contour lines. The numerical results obtained are shown graphically and compared.

Governing Equations and the Method of Solution

Consider a thin elastic plate of thickness h subject to a continuously distributed lateral load $q(x,y)$. Take the x,y plane to be the middle plane of the plate and direct the z axis perpendicular to that plane. The intersections between the deflected surface $z=w(x,y)$ and the plane $z=$const yield contours which, after projection onto the $z=0$ surface, are the level curves called "lines of equal deflection." Denote the family of such curves by $u(x,y)=$const. If the boundary c of the plate is subjected to any combination of clamping and simple support, then clearly it will belong to the family of lines of equal deflection and, without loss of generality, one may consider that $u=0$ on the boundary.

Consider the equilibrium on an element Ω_u of the plate bounded by any closed contour C_u. Equating the total downward load acting on the element to the resultant upward contribution of the tractions exerted upon this portion by the remainder, one obtains

$$\oint_{c_u} V_n \mathrm{d}s - \iint_{\Omega_u} \left(q + N_x \frac{\partial^2 w}{\partial x^2} + 2N_{xy} \frac{\partial^2 w}{\partial x \partial y} + N_y \frac{\partial^2 w}{\partial y^2} \right) \mathrm{d}x\mathrm{d}y = 0 \tag{1a}$$

Here V_n represents the transverse reactive force which contains the shearing force Q_n and the edge rate of change of the twisting moment M_{nt} along the contour; N_x, N_y, and N_{xy} represent the membrane forces acting on a small element $\mathrm{d}x\mathrm{d}y$ lying entirely within the contour C_u. Adopting Berger's approximation and substituting the well-known expressions for V_n, Q_n, and M_{nt} into Eq. (1a), as carried out in Ref. 3, one obtains

$$\frac{\mathrm{d}^3 w}{\mathrm{d}u^3} \oint_{c_u} R\mathrm{d}s + \frac{\mathrm{d}^2 w}{\mathrm{d}u^2} \oint_{c_u} F\mathrm{d}s + \frac{\mathrm{d}w}{\mathrm{d}u} \oint_{c_u} G\mathrm{d}s - \iint_{\Omega_u} (q + \alpha^2 D \nabla^2 w)\,\mathrm{d}x\mathrm{d}y = 0 \tag{1b}$$

where use has been made of the fact that W and its derivatives with respect to u are constant on the contour $u=$const. Here R, F, G, and t are the following expressions[3]

$$R = -Dt^{3/2}$$

$$F = -Dt^{1/2}\left[3u_{xx}u_x^2 + 3u_{yy}u_y^2 + u_{yy}u_x^2 + 4u_{xy}u_xu_y\right]$$

$$G = -Dt^{-3/2}\left[u_{xxx}u_x^3 u_{yyy}u_y^3 + (2-\mu)\left(u_{xxx}u_xu_y^2 + 4u_{xy}u_xu_y\right.\right.$$
$$+ u_{xyy}u_x^3 + u_{xyy}^3 u_y^3 + (2\mu-1)\left(u_{xyy}u_xu_y^2 + u_{xxy}u_x^2u_y\right)$$
$$-2(1-\mu)u_{xy}\left(u_xu_yu_{xx} - u_y^2u_{xy} - u_x^2u_{xy} + u_xu_yu_{yy}\right)$$
$$\left.\left. + (1-\mu)\left(u_{xx}-u_{yy}\right)\left(u_{xx}u_y^2 - u_{yy}u_x^2\right)\right]\right.$$
$$+2D(1-\mu)t^{-5/2}\left[u_{xy}\left(u_x^2-u_y^2\right) - u_xu_y\left(u_{xx}-u_{yy}\right)\right]^2$$

$$t = u_x^2 + u_y^2$$

where $D=Eh^3/12(1-\mu^2)$ is the flexural rigidity, E Young's modulus, and μ Poisson's ratio. The contribution of membrane forces has been replaced by $\alpha^2 D\nabla^2 W$.[5]

As a first approximation, assume the lines of equal deflection to be as for the corresponding small-amplitude deflection problem, which are a family of similar and similarly situated ellipses. Therefore we may take[3]

$$u(x,y) = 1 - (x^2/a^2) - (y^2/b^2)$$

Calculation of the values of R, F, G, and t now gives[4]

$$R = -8D/p^3$$

$$F = -4Dp\left[3\left(x^2/a^6 + y^2/b^6\right) + (1-u)/a^2b^2\right]$$

Received March 3, 1981; revision received July 27, 1981.

*Head, Department of Mathematics.